

Electronic properties of bilayer graphene with magnetic quantum structures studied using the Dirac equation

Daehan Park, Heesang Kim, and Nammee Kim*

Department of Physics, Soongsil University, Seoul 06978, Korea

(Dated: March 5, 2022)

Abstract

The electronic properties of bilayer graphene with a magnetic quantum dot and a magnetic quantum ring are investigated. The eigenenergies and wavefunctions of quasiparticle states are calculated analytically by solving decoupled fourth-order differential equations. For the magnetic quantum dot, in the case of a negative inner magnetic field, two peculiar characteristics of the eigenenergy evolution are found: (i) the energy eigenstates change in a stepwise manner owing to energy anticrossing and (ii) the quantum states approach zero energy. For the magnetic quantum ring, there is an angular momentum transition of eigenenergy as the inner radius of the ring varies, and the Aharonov–Bohm effect is observed in the eigenenergy spectra for both positive and negative magnetic fields inside the inner radius.

I. INTRODUCTION

Since the first demonstration of the fabrication of monolayer graphene [1], graphene has attracted considerable attention owing to its exotic properties, such as its long mean free path, high carrier mobility, and an anomalous quantum Hall effect [1–5]. These properties of graphene originate mainly from the existence of two independent Dirac points, which are conventionally called the K and K' valleys. In the vicinity of these valleys, graphene has a unique band structure, namely, a gapless and linear energy dispersion. As a result, electrons in graphene behave as if they were massless relativistic particles, governed by the Dirac equation.

However, these relativistic characteristics are a considerable hindrance to the realization of electronic devices based on graphene. Owing to the Klein effect [6], near-perfect transmission of Dirac electrons through an electrostatic barrier at normal incidence is possible. That is, unlike electrons in a two-dimensional electron gas (2DEG), Dirac electrons cannot be confined by an electrostatic potential. However, De Martino *et al.* [7] showed that this problem could be overcome in graphene by the application of a magnetic field. In contrast to an electrostatic potential, by deflecting the trajectory of electrons through the Lorentz force, a magnetic field allows trapping of electrons within a restricted region. Various magnetic quantum structures such as magnetic quantum dots, magnetic step barriers, and magnetic

* nammee@ssu.ac.kr

quantum rings with impurities have been investigated [7–11].

Graphene multilayers have also been widely investigated. In multilayer graphene, the layers are weakly coupled by van der Waals interaction, and its properties are very different from those of monolayer graphene. For instance, pristine bilayer graphene (BLG) exhibits gapless and parabolic energy dispersion near the K and K' valleys [12]. Also, in a uniform magnetic field B , the Landau levels (LLs) of bilayer graphene in the lowest band have a linear dependence on B , in contrast to the \sqrt{B} dependence of LLs in monolayer graphene [13].

In recent years, semiconductor-based quantum dots and quantum rings have become important subjects of study in mesoscopic physics [14]. These quantum structures have been investigated both experimentally and theoretically in BLG. There have been theoretical studies of quantum dots and quantum rings in AA-stacked [15–17], AB-stacked [18–23], and twisted [24] BLG. The properties of two or more coupled quantum dots in BLG have also been studied experimentally and theoretically [25–27]. Recently, the electronic density within BLG quantum dots has been visualized using the tip of a scanning tunneling microscope (STM) [28, 29]. The valley properties of an electrostatically confined BLG quantum dot have been investigated experimentally [30, 31], and a valley filter device based on these properties has been proposed [32].

In this paper, based on a single-particle approach, we investigate the electronic properties of BLG with two kinds of magnetic structures: a magnetic quantum dot (MQD) and a magnetic quantum ring (MQR). In most previous work on these quantum structures in a 2DEG and in monolayer graphene, there was no magnetic field inside the MQD, and the spatial area of the MQR was kept constant. Here, however, we consider the behavior of the eigenenergies of BLG as the magnetic field inside an MQD varies. We show that there are dramatic differences depending on the direction of the magnetic field inside the dot. The results for the eigenenergy spectra of BLG for an MQR with fixed spatial area reveal nothing unusual compared with the cases of a 2DEG and monolayer graphene. Therefore, we vary the inner radius of the ring and introduce antiparallel magnetic fields inside the inner circle and outside the outer circle of the ring to look for interesting phenomena that might arise.

The remainder of the paper is organized as follows. In Sec. II, we introduce a mathematical model of our magnetic quantum structures and present the mathematical solution procedure for the Hamiltonian of the BLG, including complicated boundary conditions for the fourth-order differential equations satisfied by the Dirac wavefunctions. In Sec. III A,

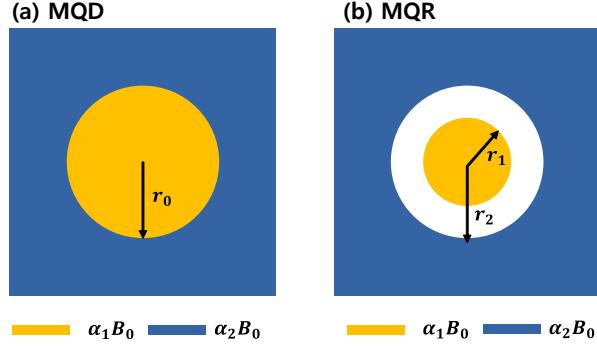


FIG. 1. Schematic geometry of (a) a magnetic quantum dot (MQD) and (b) a magnetic quantum ring (MQR).

we present our results for BLG with an MQD and discuss its energy anticrossing by using effective potentials and the probability density at subatoms. We discuss the eigenenergies and the Aharonov–Bohm effect in BLG with an MQR in Sec. III B. Finally, we summarize our results in Sec. IV.

II. MODEL AND FORMALISM

We calculate the energy spectra of BLG with an MQD or an MQR, formed by a spatially nonuniform distribution of magnetic fields, by solving the Dirac equation. The geometries of the MQD and MQR are shown schematically in Fig. 1. In Fig. 1(a), the MQD is modeled as $\vec{B} = \alpha_1 B_0 \hat{e}_z$ for $r < r_0$ and $\vec{B} = \alpha_2 B_0 \hat{e}_z$ for $r > r_0$, where $\alpha = B/B_0$ is the ratio of the applied magnetic field B to the standard magnetic field B_0 . The MQDs studied previously correspond to $\alpha_1 = 0$. In Fig. 1(b), the MQR is modeled as $\vec{B} = \alpha_1 B_0 \hat{e}_z$ for $r < r_1$, $\vec{B} = 0$ for $r_1 < r < r_2$, and $\vec{B} = \alpha_2 B_0 \hat{e}_z$ for $r > r_2$. The model of the MQD can be obtained from that for the MQR in the limit as $r_1 \rightarrow r_2$. Therefore, we shall describe the calculations for the MQR only. Because the MQR has rotational symmetry, it is convenient to use plane polar coordinates in our system. We can express the vector potential $\vec{A}(\mathbf{r})$ of the magnetic

field \vec{B} in the symmetric gauge as

$$\vec{A}(\mathbf{r}) = \begin{cases} \frac{1}{2}\alpha_1 B_0 r \hat{\theta} & \text{for } r < r_1, \\ \frac{1}{2r}\alpha_1 B_0 r_1^2 \hat{\theta} & \text{for } r_1 < r < r_2, \\ \frac{1}{2}\alpha_2 B_0 r \hat{\theta} - \frac{B_0}{2r}(\alpha_2 r_2^2 - \alpha_1 r_1^2) \hat{\theta} & \text{for } r > r_2. \end{cases} \quad (1)$$

The Hamiltonian for BLG with Bernal (AA) stacking near the K valley is given by [12]

$$H = \begin{pmatrix} 0 & \pi & t_\perp & 0 \\ \pi^\dagger & 0 & 0 & 0 \\ t_\perp & 0 & 0 & \pi^\dagger \\ 0 & 0 & \pi & 0 \end{pmatrix}, \quad (2)$$

where $\pi = \Pi_x + i\Pi_y$, $\pi^\dagger = \Pi_x - i\Pi_y$, $\Pi_i = v_F[p_i + (e/c)A_i]$, the Fermi velocity $v_F \approx c/300$, $t_\perp = 400$ meV is an interlayer hopping parameter, and c is the speed of light. The wavefunctions of the Hamiltonian in Eq. (2) can be expressed as a four-spinor wavefunction $\vec{\psi} = (\psi_A, \psi_B, \psi_{B'}, \psi_{A'})^T$. In our system, the vector potentials have spatial circular symmetry, and thus this four-spinor wavefunction can be written as [18]

$$\vec{\psi} = e^{im\theta} (\phi_A(r), ie^{-i\theta}\phi_B(r), \phi_{B'}(r), ie^{i\theta}\phi_{A'}(r))^T, \quad (3)$$

where m is an angular momentum quantum number. To simplify our problem, we nondimensionalize quantities by taking the unit of length to be the magnetic length $l_B = \sqrt{2\hbar/eB_0}$ and the unit of energy to be $\epsilon_0 = \sqrt{2}\hbar v_F/l_B$. For a standard magnetic field $B_0 = 10$ T, the values of l_B and ϵ_0 are 11.4 nm and 81.05 meV, respectively.

In dimensionless units, by solving the Dirac equation, $(H - E)\vec{\psi} = 0$, we obtain the following four coupled first-order differential equations:

$$\left[\frac{d}{dr} - \frac{m-1}{r} - v(r) \right] \phi_B = \sqrt{2}(\epsilon\phi_A - t\phi_{B'}), \quad (4)$$

$$\left[\frac{d}{dr} + \frac{m}{r} + v(r) \right] \phi_A = -\sqrt{2}\epsilon\phi_B, \quad (5)$$

$$\left[\frac{d}{dr} + \frac{m+1}{r} + v(r) \right] \phi_{A'} = \sqrt{2}[\epsilon\phi_{B'}(r) - t\phi_A], \quad (6)$$

$$\left[\frac{d}{dr} - \frac{m}{r} - v(r) \right] \phi_{B'} = -\sqrt{2}\epsilon\phi_{A'}, \quad (7)$$

where $t = t_\perp/\epsilon_0 = 4.96$. The expressions for $v(r)$ in each region are as follows:

$$v(r) = \begin{cases} \alpha_1 r & \text{for } r < r_1, \\ \frac{\alpha_1 r_1^2}{r} & \text{for } r_1 < r < r_2, \\ \alpha_2 r - \frac{\alpha_2 r_2^2 - \alpha_1 r_1^2}{r} & \text{for } r_2 < r. \end{cases} \quad (8)$$

Therefore, we need to solve four coupled first-order differential equations. Fortunately, however, Eqs (4)–(7) can be decoupled to give a fourth-order differential equation for $\phi_A(r)$ in each region:

in region I ($r < r_1$),

$$\left[\frac{d^2}{dr^2} + \frac{1}{r} \frac{d}{dr} - \frac{m^2}{r^2} - 2\alpha_1 m - \alpha_1^2 r^2 + 2\epsilon^2 \right]^2 \phi_A^I = 4(\alpha^2 + t^2 \epsilon^2) \phi_A^I, \quad (9)$$

in region II ($r_1 < r < r_2$),

$$\left[\frac{d^2}{dr^2} + \frac{1}{r} \frac{d}{dr} - \frac{m_2^2}{r^2} + 2\epsilon^2 \right]^2 \phi_A^{II} = 4t^2 \epsilon^2 \phi_A^{II}, \quad (10)$$

in region III ($r_2 < r$),

$$\left[\frac{d^2}{dr^2} + \frac{1}{r} \frac{d}{dr} - \frac{m_3^2}{r^2} - 2\alpha_2 m_3 - \alpha_2^2 r^2 + 2\epsilon^2 \right]^2 \phi_A^{III} = 4(\alpha^2 + t^2 \epsilon^2) \phi_A^{III}, \quad (11)$$

where m_2 and m_3 are $m + \alpha_1 s_1$ and $m - (\alpha_2 s_2 - \alpha_1 s_1)$, respectively. Here, $\alpha_1 s_1 = \pi \alpha_1 B_0 r_1^2 / \phi_0$ and $\alpha_2 s_2 = \pi \alpha_2 B_0 r_2^2 / \phi_0$ are the numbers of magnetic flux quanta inside $r < r_1$ and $r < r_2$, respectively, where $\phi_0 = h/e$ is a flux quantum and $r_i = \sqrt{s_i}$ in dimensionless units.

The solutions of Eqs. (9)–(11) for ϕ_A are

$$\phi_A(r) = \begin{cases} r^{|m|} e^{-\alpha_1 r^2/2} [AM(\delta_+^1, |m| + 1, \alpha_1 r^2) + BM(\delta_-^1, |m| + 1, \alpha_1 r^2)] & \text{for } r < r_1, \\ C_1 J_{|m_2|}(\sqrt{2}\gamma_+ r) + D_1 N_{|m_2|}(\sqrt{2}\gamma_+ r) + C_2 J_{|m_2|}(\sqrt{2}\gamma_- r) + D_2 N_{|m_2|}(\sqrt{2}\gamma_- r) & \text{for } r_1 < r < r_2, \\ r^{|m_3|} e^{-\alpha_2 r^2/2} [EU(\delta_+^2, |m_3| + 1, \alpha_2 r^2) + FU(\delta_-^2, |m_3| + 1, \alpha_2 r^2)] & \text{for } r_2 < r, \end{cases} \quad (12)$$

where

$$\delta_{\pm}^i = -\frac{\beta_{i,\pm}^2}{2\alpha_i} + \frac{1}{2} \left(|m| + \frac{\alpha_i}{|\alpha_i|} m + 1 \right), \quad \beta_{i,\pm} = \sqrt{\epsilon^2 \pm \sqrt{\alpha_i^2 + (t\epsilon)^2}}, \quad \gamma_{\pm} = \sqrt{\epsilon^2 \pm t\epsilon},$$

M and U are confluent hypergeometric functions, and J_m and N_m are Bessel functions of the first and second kinds, respectively. The wavefunctions for the other subatoms, namely, ϕ_B , $\phi_{A'}$, and $\phi_{B'}$, can also be derived from Eqs. (4)–(7). Unlike the Schrödinger equation and the Dirac equation for monolayer graphene, the equations for ϕ_A for BLG are fourth-order differential equations. Therefore, we need to derive appropriate boundary conditions for ϕ_A . These boundary conditions can be obtained from the continuity of the wavefunctions for all subatoms, ϕ_A , ϕ_B , $\phi_{A'}$, and $\phi_{B'}$, at the boundaries as follows:

at $r = r_1$, which is the boundary between regions I and II,

$$\phi_A^I(r_1) - \phi_A^{II}(r_1) = 0 \quad (13)$$

$$\left. \frac{d}{dr} \phi_A^I \right|_{r_1} - \left. \frac{d}{dr} \phi_A^{II} \right|_{r_1} = 0, \quad (14)$$

$$\left. \frac{d^2}{dr^2} \phi_A^I \right|_{r_1} + 2\alpha_1 \phi_A^I(r_1) - \left. \frac{d^2}{dr^2} \phi_A^{II} \right|_{r_1} = 0, \quad (15)$$

$$\begin{aligned} \left. \frac{d^3}{dr^3} \phi_A^I \right|_{r_1} - \left. \frac{d^3}{dr^3} \phi_A^{II} \right|_{r_1} + 2\alpha_1 \left. \frac{d}{dr} \phi_A^I \right|_{r_1} \\ - \frac{2\alpha_1 + 4\alpha_1(m + \alpha_1 r_1^2)}{r_1} \phi_A^I(r_1) = 0, \end{aligned} \quad (16)$$

and at $r = r_2$, which is the boundary between regions II and III,

$$\phi_A^{III}(r_2) - \phi_A^{II}(r_2) = 0, \quad (17)$$

$$\left. \frac{d}{dr} \phi_A^{III} \right|_{r_2} - \left. \frac{d}{dr} \phi_A^{II} \right|_{r_2} = 0, \quad (18)$$

$$\left. \frac{d^2}{dr^2} \phi_A^{III} \right|_{r_2} + 2\alpha_2 \phi_A^{III}(r_2) - \left. \frac{d^2}{dr^2} \phi_A^{II} \right|_{r_2} = 0, \quad (19)$$

$$\begin{aligned} \left. \frac{d^3}{dr^3} \phi_A^{III} \right|_{r_2} - \left. \frac{d^3}{dr^3} \phi_A^{II} \right|_{r_2} + 2\alpha_2 \left. \frac{d}{dr} \phi_A^{III} \right|_{r_2} \\ - \left(\frac{2\alpha_2}{r_2} + \frac{m_2^2 - m_3^2}{r_2^3} + 2\alpha_2^2 r_2 \right) \phi_A^{III}(r_2) = 0. \end{aligned} \quad (20)$$

The corresponding eigenenergies of an MQR in BLG can be obtained by finding the roots of the secular equations obtained from the boundary conditions.

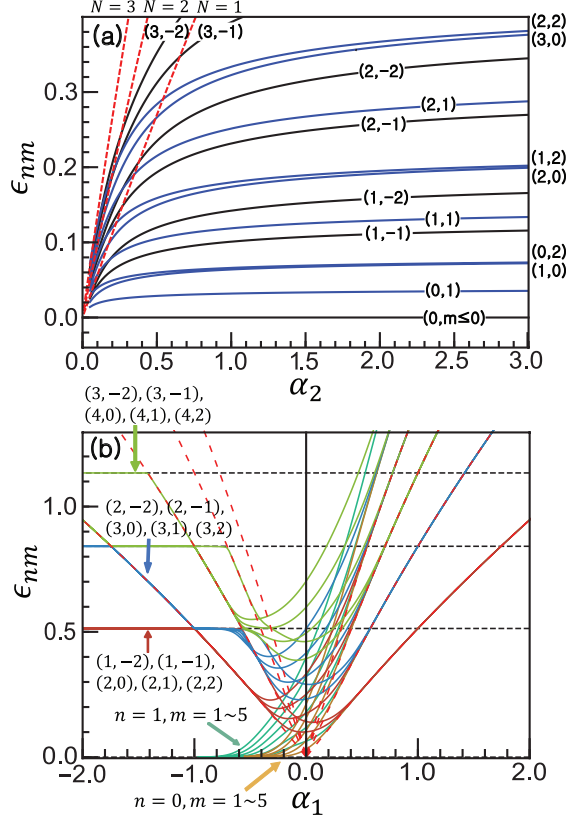


FIG. 2. Eigenenergies ϵ_{nm} of BLG with an MQD: (a) ϵ_{nm} as functions of α_2 with $\alpha_1 = 0$; (b) ϵ_{nm} as functions of α_1 with $\alpha_2 = 1.0$.

III. RESULTS AND DISCUSSION

A. Magnetic quantum dot

In this subsection, we discuss the electronic properties of BLG with an MQD. In Figs. 2(a) and 2(b), the eigenenergies ϵ_{nm} are plotted as functions of α_2 and α_1 , respectively, for two different MQD cases. The radius r_0 of the MQD is 5 in dimensionless units. In the quantum state (n, m) , n is the number of nodes in the radial wavefunction and m is the angular momentum quantum number. First of all, to allow comparisons with the typical MQDs considered in previous work based on a 2DEG model, we consider the case in which the inside magnetic field α_1 of MQD is zero and the outside magnetic field α_2 varies. The results are shown in Fig. 2(a). There is a noticeable difference in that we have zero-energy states for the MQD in BLG. These zero-energy states are also present for an MQD in monolayer graphene. The red dashed lines in the figure represent the dimensionless Landau

levels (LLs) for BLG [33], i.e.,

$$\sqrt{2\alpha} \sqrt{\frac{t^2/\alpha+4N+2}{4}} - \sqrt{\left(\frac{t^2/\alpha+4N+2}{4}\right)^2 - N(N+1)},$$

where N is the Landau index corresponding to $n + (m + |m|)/2$ in our calculation. For a magnetic field that is weak compared with t , the LLs are approximately proportional to B . Except for these features, the energy spectra of BLG with a typical MQD show the general characteristics of an MQD in the 2DEG case [7, 34, 35]. For a small outer magnetic field α_2 , the wavefunctions are mostly distributed outside the MQD, as a consequence of which the energies are close to the LLs of BLG. On the other hand, as α_2 increases, the cyclotron radius of the electrons becomes smaller than the radius of the dot, and the energies start to deviate from the LLs. Because the Lorentz force leads to strong localization of the electrons within MQD, the energy evolution is very similar to that of an MQD in the 2DEG case. These energy changes are also the same as for a conventional circular dot that is electrostatically confined by hard walls without magnetic fields.

In Fig. 2(b), the inside magnetic field α_1 varies, while the outside magnetic field is fixed at $\alpha_2 = 1$. The LLs inside the MQD (red dashed lines) are fan-shaped because α_1 increases, and the LLs outside the MQD (black dashed lines) are flat because α_2 remains constant. When α_1 increases in the positive direction, the wavefunctions are localized within the MQD. Thus, the eigenenergies approach the LLs inside the MQD. However, when α_1 becomes negative, the evolution of the eigenenergy exhibits two peculiar characteristics: (i) the eigenenergies converge to the LLs outside the dot in a stepwise manner through energy anticrossing; (ii) the eigenenergies of some quantum states approach zero energy. We now consider these characteristics in greater detail.

To explain the stepped shape of the energy evolution for a negative inner magnetic field α_1 , in Fig. 3 we plot ϵ_{nm} as functions of negative α_1 , the effective potential of MQD for $m = 0$, and the probability density of a given quantum state (n, m) .

In Fig. 3(a), the red dashed lines and black dashed lines indicate the LLs inside and outside the MQD, respectively. The $(0, 0)$ state has zero energy regardless of $|\alpha_1|$, and the $(1, 0)$ state tends to zero energy as $|\alpha_1|$ increases. The eigenenergies ($n \geq 2, 0$) are determined by one of the LLs inside or outside the MQD, depending on the value of α_1 . For small α_1 near zero, the wavefunctions are located mainly at the boundary of the MQD, and the eigenenergies deviate from the LLs both inside and outside the MQD. However, as $|\alpha_1|$

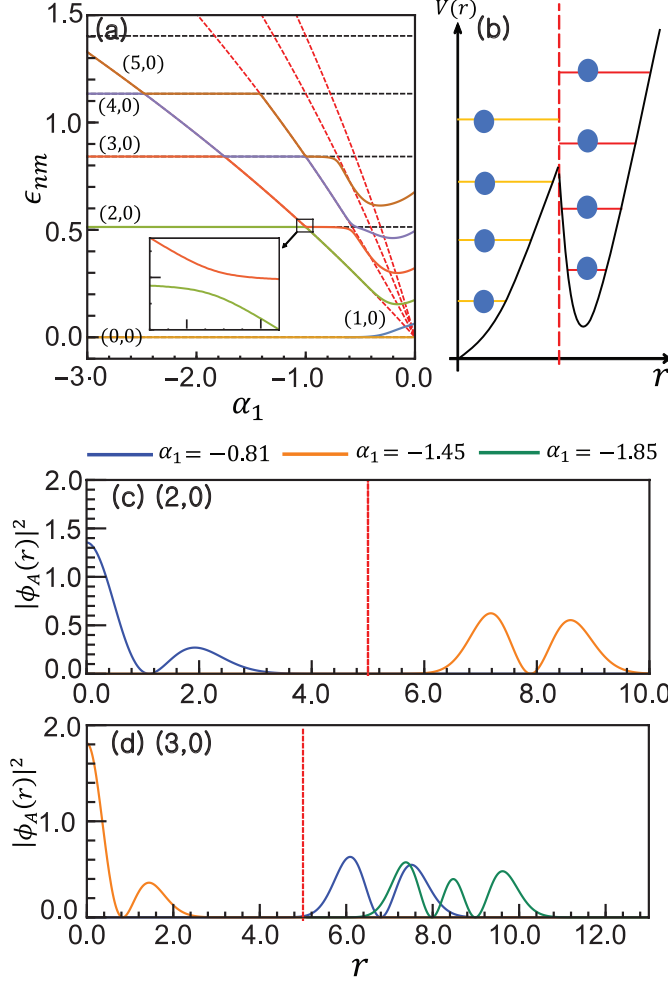


FIG. 3. Characteristics of BLG with an MQD with negative inner magnetic field α_1 . (a) Eigenenergies ϵ_{nm} as functions of negative α_1 for $m = 0$. The inset shows energy anticrossing between two LLs. (b) Schematic of effective potential for $m = 0$. (c) and (d) probability densities $|\phi_A(r)|^2$ for the $(2,0)$ and $(3,0)$ states, respectively. The red dashed lines in (b)–(d) indicate the radius r_0 . All the wavefunctions are normalized.

starts to increase, the wavefunctions move to the inside of the MQD and are affected by the inside magnetic field α_1 , and the energies start to follow the LLs inside the MQD. When an LL inside the MQD becomes equal to an LL outside the MQD, a state following an LL inside the MQD transitions to an LL outside the MQD, and vice versa. At such a time, energy anticrossing occurs, as shown in the inset in Fig. 3(a). These anticrossing phenomena are also found in electrostatically confined quantum dots and rings in monolayer graphene and BLG [17, 20, 36].

Figure 3(b) is a qualitative representation of the effective potential for the $m = 0$ state of BLG with an MQD. We shall explain these anticrossing phenomena in terms of the effective potential. If whole wavefunctions can be localized either inside or outside the MQD, we can simply assume that the system energies are determined only by the LLs in the respective region. As the magnetic field α_1 increases, the energy-level spacing inside the MQD becomes wider, and the energy levels start to become equal to the LLs outside the MQD. When the first LL inside the MQD becomes higher than the first LL outside the MQD, to maintain the energy level sequence for a fixed m , the state with the first LL inside the MQD moves to the first LL outside the MQD. Therefore, energy anticrossing occurs whenever LLs in the two different regions become the same. As the magnetic field increases, the wavefunction moves back and forth between the outside and inside of the MQD until the first inside LL becomes larger than the other fixed outside LLs, and, as a result, the wavefunctions of all states are located outside the MQD.

The $(2, 0)$ state experiences energy anticrossing once and the $(3, 0)$ state three times in the region $0 < |\alpha_1| < 3$, as shown in Fig. 3(a). To explain the alternating movement of wavefunctions as the magnetic field inside the MQD varies, we show the probabilities densities of the wavefunctions for the $(2, 0)$ and $(3, 0)$ states in Figs. 3(c) and 3(d), respectively. For the $(2, 0)$ state, the wavefunction moves from inside the MQD at $\alpha_1 = -0.81$ to outside it at $\alpha_1 = -1.45$ [Fig. 3(c)]. For the $(3, 0)$ state, the wavefunction moves from outside the MQD at $\alpha_1 = -0.81$ to inside it at $\alpha_1 = -1.45$, and then moves out again at $\alpha_1 = -1.85$ [Fig. 3(d)]. Before and after energy anticrossing occurs, the probability densities are located alternately inside and outside the MQD.

It is known that in monolayer graphene and BLG in a uniform magnetic field, wavefunctions of states at the zero Landau energy are completely localized in a particular subatom [13]. For the opposite magnetic field direction, the wavefunctions are all localized in the other subatom. In the present study, we consider a nonuniform magnetic field, and the magnetic field inside the MQD is opposite to that outside it. We would like to check if wavefunction separation occurs in this case as well. In Fig. 4, we plot the probability density of different subatoms for $\alpha_1 = -0.25$, 0.00, and +0.61. For $\alpha_1 = +0.61$ (green lines), the $(0, 1)$ state has nonzero eigenenergy, and the probability densities of all subatoms are located within the MQD in Figs. 4(a)–4(d). There is no wavefunction separation. For $\alpha_1 = 0.00$ (orange lines), in Figs. 4(a) and 4(b), the probability densities of the A and A' subatoms

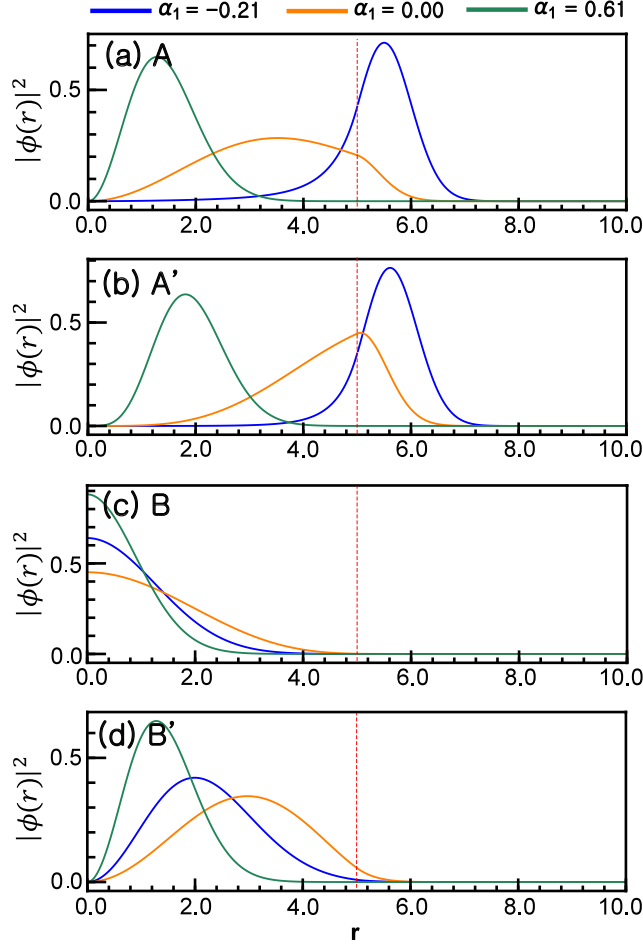


FIG. 4. Probability density $|\psi(r)|^2$ for subatoms A , B , A' , and B' in the $(0, 1)$ state for different magnetic fields $\alpha_1 = -0.21$, 0.00 , and $+0.61$. To allow comparison, all the wavefunctions are normalized. The red dotted lines indicate the radius r_0 .

are distributed over the MQD boundary, while in Figs. 4(c) and 4(d), the wavefunctions of the B and B' subatoms are localized inside the MQD. There is still no clear wavefunction separation. Now, for $\alpha_1 = -0.21$ (blue lines), this state approaches zero energy, and the wavefunctions of the A and A' subatoms are mainly located outside the MQD, as shown in Figs. 4(a) and 4(b), while the wavefunctions of the B and B' subatoms are more strongly localized within the MQD than those for $\alpha_1 = 0.00$, as shown in Figs. 4(c) and 4(d). As a result, $|\phi_A|^2$ and $|\phi_{A'}|^2$ are distributed in a ring shape along the MQD boundary, while $|\phi_B|^2$ and $|\phi_{B'}|^2$ are distributed inside the MQD. The $(n, m \geq 0)$ states, where $n = 0, 1$, tend toward zero energy, because the wavefunctions of each subatom start to be separated when α_1 increases in the negative direction. From these results, we can infer that wavefunction

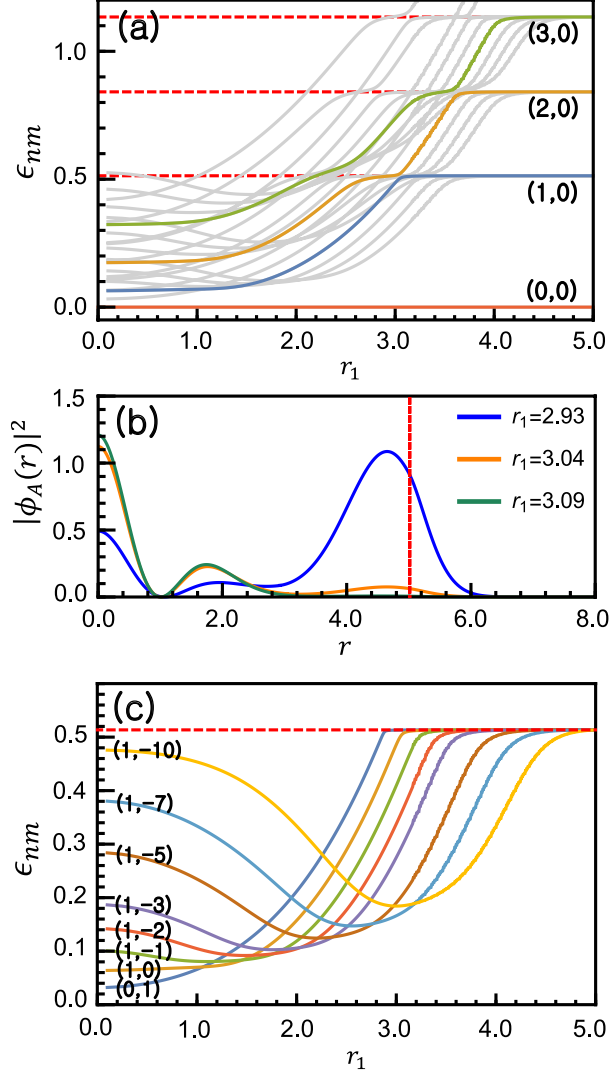


FIG. 5. (a) Eigenenergies ϵ_{nm} as functions of r_1 for an MQR in BLG. Colored lines are for the state with $m = 0$, and gray lines represent other states (n, m) , where $n \in [-2, 2]$ and $m \in [-3, 3]$. Red dashed lines show the LLs of BLG. (b) Probability densities $|\psi(r)|^2$ of the $(1, 0)$ state for different values of r_1 near energy anticrossing. The red dashed line indicates the outer radius r_2 of the ring. (c) ϵ_{nm} as a function of r_1 in the region of $\epsilon_{nm} < 0.5$ for the $(1, m)$ states.

separation also occurs for zero-eigenenergy states in BLG, even with a nonuniform magnetic field distribution.

B. Magnetic quantum ring

In this subsection, we discuss the electronic properties of BLG with an MQR. For a fixed ring area with parallel magnetic fields ($\alpha_1 = \alpha_2$), the results for the eigenenergy spectra show nothing unusual compared with the cases of 2DEG and monolayer graphene [34, 37–39]. Here, we investigate BLG with an MQR from a different perspective.

First, we investigate the eigenenergies by varying the inner radius r_1 of the MQR with parallel magnetic fields ($\alpha_1 = \alpha_2$). We fix the outer radius of the MQR as $r_2 = 5$. The results are presented in Fig. 5. In Fig. 5(a), the eigenenergies ϵ_{nm} are shown as functions of r_1 . The eigenenergy of the (1,0) state (blue line) increases until it converges to the LL ($n = 1$) inside the ring as r_1 increases. The eigenenergy of the (2,0) state (orange line) exhibits a similar tendency, and it converges to the LL ($n = 2$) inside the ring through energy anticrossing near the LL ($n = 1$), as shown in Fig. 5(a). The average kinetic energy of an electron in a magnetic field is higher than in the absence of the field. Increasing the inner radius r_1 causes a decrease in the missing magnetic flux in the ring area, and so the eigenenergies of the BLG increase.

To explain the wavefunction movement near anticrossing, in Fig. 5(b), we plot the probability density distribution of the (1,0) state as a function of r for different values of the inner ring radius r_1 . For $r_1 = 2.93$ (blue lines) before anticrossing, the wavefunction is distributed widely over the MQR. For $r_1 = 3.09$ (green lines) after anticrossing, the wavefunction is localized inside the inner circle of the MQR. The energy converges to the LL ($n = 1$) inside the ring when $r_1 > 3.04$. This anticrossing can be explained using the same arguments as in the MQD case. At anticrossing, the size of the inner magnetic field region is large enough to encompass the wavefunctions of all subatoms for a lower energy. The wavefunctions within the ring move to the inner magnetic field region ($r_1 < r$), while a part of the wavefunction for higher energy moves to the ring region $r_1 < r < r_2$. Before and after energy anticrossing occurs, the wavefunctions are alternately located in regions with $B = 0$ and $B \neq 0$ (inside the inner circle or outside the outer circle) of the MQR.

To study the angular momentum transition as the inner radius of the MQR varies, in Fig. 5(c), we plot ϵ_{nm} as functions of r_1 in the region $\epsilon_{nm} < 0.5$ for the (1, m) states. For an MQR with a finite width and for a conventional quantum ring confined by an electrostatic potential, an angular momentum transition is observed with increasing magnetic field [18,

34, 37]. When the size of the ring is fixed, this transition is due mainly to the missing flux quanta in the ring area. However, in the present study, an angular momentum transition is observed with increasing inner ring radius r_1 for a fixed magnetic field. As the inner ring radius increases, the number of missing flux quanta in the ring area ($r_1 < r < r_2$) decreases, but the number of flux quanta within the inner ring radius increases. The small value of m leads to rapid recovery of the LL as the inner circle radius r_1 increases. From the existence of this phenomenon, we can infer that the angular momentum transition depends more on the inner circle flux quanta than on the missing flux quanta in the ring area. The argument based on missing flux quanta is only valid when the ring area remains constant.

In Fig. 6, we show the eigenenergies ϵ_{nm} of BLG with an MQR as functions of α_1 for fixed $r_1 = 3$, $r_2 = 5$, and $\alpha_2 = 1$. Here, we change the magnetic field α_1 of the inner circle. As we vary α_1 from -1.5 to $+1.5$, we can see the energy spectra of the MQR in parallel magnetic fields as well as in antiparallel fields. The energies of the $(0, m \geq 0)$ and $(1, m \geq 0)$ states of the MQR approach zero, similarly to what happens for the MQD, although the states of the MQR reach zero energy at a larger $|\alpha_1|$ value than those of the MQD. Geometrically, the difference between an MQD and an MQR is the presence in the latter of the zero-magnetic-field region $r_1 < r < r_2$. This difference is responsible for the very different behavior of ϵ_{nm} .

For conventional quantum rings (CQRs) formed by an electrostatic potential or by an etched boundary and based on a 2DEG and monolayer graphene, the Aharonov–Bohm (AB) effect has been studied both theoretically and experimentally [14, 40–44]. On the other hand, little attention has been paid to the AB effect for an MQR in a 2DEG. In a CQR, the energy of an electron bound in the ring oscillates as a function of the magnetic flux ϕ inside the ring. We find that the energy dispersion of BLG with an MQR also exhibits this effect for both large positive and large negative values of $|\alpha_1|$. To investigate the AB effect for an MQR, we calculate the period of the magnetic flux $\Delta\phi$ of the MQR numerically, and we find that this period is close to ϕ_0 : for $\alpha_1 < 0$, it is $1.01\phi_0$, and for $\alpha_1 > 0$, it is $0.97\phi_0$. For small α_1 , the wavefunctions are not well localized in the ring region. Thus, the AB effect is not clearly seen in the range between $\alpha_1 = -0.5$ and $\alpha_1 = 0.5$. However, as $|\alpha_1|$ increases, the quantum states start to be strongly localized in the ring region, and exhibit an obvious AB effect. Unlike CQRs, whose energy has symmetry with regard to the direction of the magnetic flux inside the ring [14], the energy in our case does not possess such symmetry,

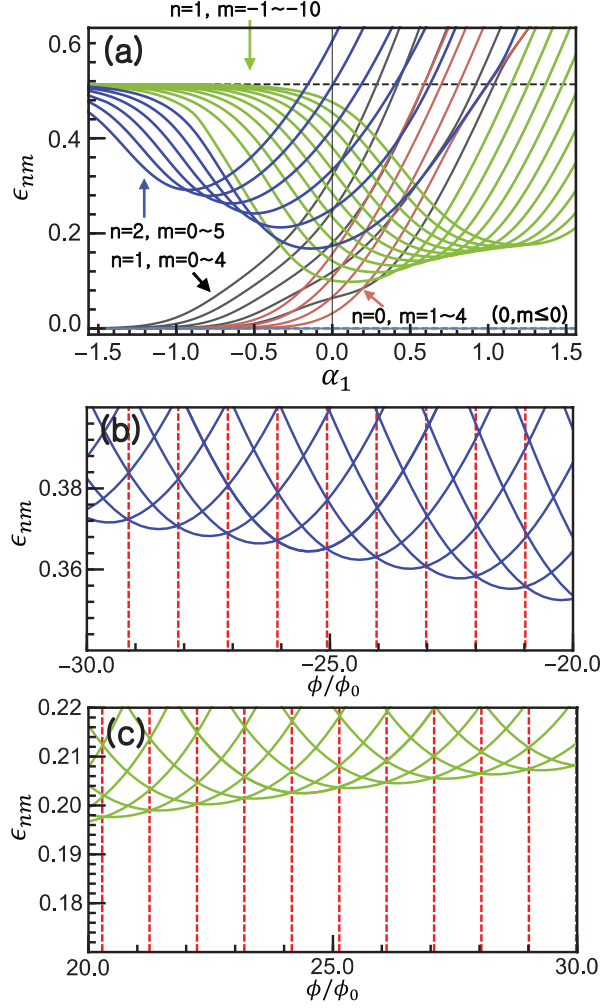


FIG. 6. Energy spectra of BLG with an MQR. The inner radius r_1 and outer radius r_2 of the MQR are 3 and 5, respectively. (a) Eigenenergies ϵ_{nm} as functions of α_1 . (b) Eigenenergies ϵ_{nm} of the states $(2, m)$, with $m \in [16, 25]$ as functions of magnetic flux. (c) Eigenenergies ϵ_{nm} of the states $(1, m)$, with $m \in [-20, -30]$, as functions of magnetic flux.

because our MQR is formed by a nonuniform magnetic field. We believe that this AB effect should also be seen in MQRs based on a 2DEG or monolayer graphene.

IV. CONCLUSION

In this paper, we have analytically studied the electronic properties of bilayer graphene (BLG) with a magnetic quantum dot (MQD) and a magnetic quantum ring (MQR). We have calculated eigenenergies and wavefunctions based on a continuum model of the BLG

using the Dirac equation. In contrast to previous studies, we have considered as significant variables the nonzero magnetic field inside the quantum dot, the size of the dot, the radius of the inner ring, and the directions of the magnetic fields inside the inner ring and outside the outer ring.

For the MQD, as the inside magnetic field increases in the positive direction, the corresponding eigenenergies of the BLG approach the Landau levels (LLs) inside the dot, and its states are localized inside the dot. However, when the magnetic field inside the dot has the opposite direction to that outside the dot, we see two characteristic features. The first is a stepwise evolution of states through energy anticrossing. The second is that there are quantum states approaching zero energy. In these zero-energy states, the wavefunctions at each subatom are separated to lie either inside or outside the MQD. We explain these characteristics by using an effective potential and a separation of the wavefunction probability density.

For the MQR, an angular momentum transition occurs when r_1 is varied, and this transition depends more on the magnetic flux inside the inner circle of the ring than on the missing flux quanta in the ring area. For a negative magnetic flux α_1 , the MQR behaves similarly to the MQD, with some quantum states approaching zero energy, although the critical value of α_1 associated with zero energy is larger than in the case of an MQD. We have investigated the Aharonov–Bohm effect on energy spectra of the MQR. For a large magnetic flux inside the ring, the period of the Aharonov–Bohm effect in the ring is close to the value of the magnetic flux quantum ϕ_0 .

We believe that our results here could be helpful as a basis for further study of quantum transport in BLG with these magnetic quantum structures.

ACKNOWLEDGMENTS

This work was supported by Basic Science Research Program through National Research Foundation of Korea(NRF) funded by the Ministry of Science and ICT (Grant No. NRF-

2019R1A2C1088327) and the Ministry of Education (Grant No. NRF-2018R1D1A1B07046338).

- [1] K. S. Novoselov, A. K. Geim, S. V. Morozov, D. Jiang, Y. Zhang, S. V. Dubonos, I. V. Grigorieva, and A. A. Firsov, *Science* **306**, 666 (2004).
- [2] K. S. Novoselov, A. K. Geim, S. V. Morozov, D. Jiang, M. I. Katsnelson, I. V. Grigorieva, S. V. Dubonos, and A. A. Firsov, *Nature* **438**, 197 (2005).
- [3] P. J. Zomer, S. P. Dash, N. Tombros, and B. J. van Wees, *Appl. Phys. Lett.* **99**, 232104 (2011).
- [4] V. P. Gusynin and S. G. Sharapov, *Phys. Rev. Lett.* **95**, 146801 (2005).
- [5] Y. Zhang, Y.-W. Tan, H. L. Stormer, and P. Kim, *Nature* **438**, 201 (2005).
- [6] O. Klein, *Z. Phys.* **53**, 157 (1929).
- [7] A. De Martino, L. Dell’Anna, and R. Egger, *Phys. Rev. Lett.* **98**, 066802 (2007).
- [8] A. De Martino, L. Dell’Anna, and R. Egger, *Solid State Commun.* **144**, 547 (2007).
- [9] D. Wang and G. Jin, *Phys. Lett. A* **373**, 4082 (2009).
- [10] M. Ramezani Masir, A. Matulis, and F. M. Peeters, *Phys. Rev. B* **79**, 155451 (2009).
- [11] C. M. Lee, K. S. Chan, and J. C. Y. Ho, *J. Phys. Soc. Jpn.* **83**, 034007 (2014).
- [12] E. McCann and M. Koshino, *Rep. Prog. Phys.* **76**, 056503 (2013).
- [13] M. Nakamura, L. Hirasawa, and K.-I. Imura, *Phys. Rev. B* **78**, 033403 (2008).
- [14] A. Fuhrer, S. Lüscher, T. Ihn, T. Heinzel, K. Ensslin, W. Wegscheider, and M. Bichler, *Nature* **413**, 822 (2001).
- [15] Y. Zahidi, A. Belouad, and A. Jellal, *Mater. Res. Express* **4**, 055603 (2017).
- [16] A. Belouad, Y. Zahidi, and A. Jellal, *Mater. Res. Express* **3**, 055005 (2016).
- [17] H. S. Qasem, H. M. Abdullah, M. A. Shukri, H. Bahlouli, and U. Schwingenschlögl, *Phys. Rev. B* **102**, 075429 (2020).
- [18] J. M. Pereira, P. Vasilopoulos, and F. M. Peeters, *Nano Lett.* **7**, 946 (2007).
- [19] J. M. Pereira, F. M. Peeters, P. Vasilopoulos, R. N. Costa Filho, and G. A. Farias, *Phys. Rev. B* **79**, 195403 (2009).
- [20] M. Zarenia, J. M. Pereira, F. M. Peeters, and G. A. Farias, *Nano Lett.* **9**, 4088 (2009).
- [21] M. Zarenia, J. M. Pereira, A. Chaves, F. M. Peeters, and G. A. Farias, *Phys. Rev. B* **81**, 045431 (2010).
- [22] D. da Costa, M. Zarenia, A. Chaves, G. Farias, and F. Peeters, *Carbon* **78**, 392 (2014).

- [23] D. R. da Costa, M. Zarenia, A. Chaves, G. A. Farias, and F. M. Peeters, *Phys. Rev. B* **93**, 085401 (2016).
- [24] A. Tiutiunnyk, C. Duque, F. Caro-Lopera, M. Mora-Ramos, and J. Correa, *Physica E* **112**, 36 (2019).
- [25] L. Banszerus, S. Möller, E. Icking, K. Watanabe, T. Taniguchi, C. Volk, and C. Stampfer, *Nano Lett.* **20**, 2005 (2020).
- [26] M. Eich, R. Pisoni, A. Pally, H. Overweg, A. Kurzmann, Y. Lee, P. Rickhaus, K. Watanabe, T. Taniguchi, K. Ensslin, and T. Ihn, *Nano Lett.* **18**, 5042 (2018).
- [27] D. P. Żebrowski, F. M. Peeters, and B. Szafran, *Phys. Rev. B* **96**, 035434 (2017).
- [28] Z. Ge, F. Joucken, E. Quezada, D. R. da Costa, J. Davenport, B. Giraldo, T. Taniguchi, K. Watanabe, N. P. Kobayashi, T. Low, and J. Velasco, *Nano Lett.* **20**, 8682 (2020).
- [29] J. Velasco, J. Lee, D. Wong, S. Kahn, H.-Z. Tsai, J. Costello, T. Umeda, T. Taniguchi, K. Watanabe, A. Zettl, F. Wang, and M. F. Crommie, *Nano Lett.* **18**, 5104 (2018).
- [30] A. Kurzmann, M. Eich, H. Overweg, M. Mangold, F. Herman, P. Rickhaus, R. Pisoni, Y. Lee, R. Garreis, C. Tong, K. Watanabe, T. Taniguchi, K. Ensslin, and T. Ihn, *Phys. Rev. Lett.* **123**, 026803 (2019).
- [31] M. Eich, F. Herman, R. Pisoni, H. Overweg, A. Kurzmann, Y. Lee, P. Rickhaus, K. Watanabe, T. Taniguchi, M. Sigrist, T. Ihn, and K. Ensslin, *Phys. Rev. X* **8**, 031023 (2018).
- [32] Z. Hou, Y.-F. Zhou, X. C. Xie, and Q.-F. Sun, *Phys. Rev. B* **99**, 125422 (2019).
- [33] J. M. Pereira, F. M. Peeters, and P. Vasilopoulos, *Phys. Rev. B* **76**, 115419 (2007).
- [34] S. Lee, S. Souma, G. Ihm, and K. Chang, *Phys. Rep.* **394**, 1 (2004).
- [35] H.-S. Sim, K.-H. Ahn, K. J. Chang, G. Ihm, N. Kim, and S. J. Lee, *Phys. Rev. Lett.* **80**, 1501 (1998).
- [36] G. Giavaras and F. Nori, *Appl. Phys. Lett.* **97**, 243106 (2010).
- [37] N. Kim, G. Ihm, H.-S. Sim, and K. J. Chang, *Phys. Rev. B* **60**, 8767 (1999).
- [38] G. Li, N. Yang, W. Chu, H. Song, and J.-L. Zhu, *Phys. Lett. A* **383**, 125865 (2019).
- [39] D. H. Park and N. Kim, *J. Korean Phys. Soc* **77**, 1233 (2020).
- [40] R. Farghadan, A. Saffarzadeh, and E. Heidari Semiromi, *J. Appl. Phys.* **114**, 214314 (2013).
- [41] D. R. da Costa, A. Chaves, M. Zarenia, J. M. Pereira, G. A. Farias, and F. M. Peeters, *Phys. Rev. B* **89**, 075418 (2014).
- [42] D. J. P. de Sousa, A. Chaves, J. M. Pereira, and G. A. Farias, *J. Appl. Phys.* **121**, 024302

(2017).

- [43] S. Russo, J. B. Oostinga, D. Wehenkel, H. B. Heersche, S. S. Sobhani, L. M. K. Vandersypen, and A. F. Morpurgo, Phys. Rev. B **77**, 085413 (2008).
- [44] P. Recher, B. Trauzettel, A. Rycerz, Y. M. Blanter, C. W. J. Beenakker, and A. F. Morpurgo, Phys. Rev. B **76**, 235404 (2007).